




Effect of Gd content on the discharge and electrochemical behaviors of the magnesium alloy AZ31 as an anode for Mg-air battery

Quan Li¹, Wei Xiong^{1*} , Sirong Yu¹, Ying Liu¹, Jing Li¹, Lin Liu¹, Xiaojian Bi¹, Guang Zhu¹, Enyang Liu¹, Yan Zhao¹, and Bingying Wang¹

¹School of Materials Science and Engineering, China University of Petroleum (East China), Qingdao 266580, China

Received: 9 March 2021

Accepted: 23 April 2021

Published online:

10 May 2021

© The Author(s), under exclusive licence to Springer Science+Business Media, LLC, part of Springer Nature 2021

ABSTRACT

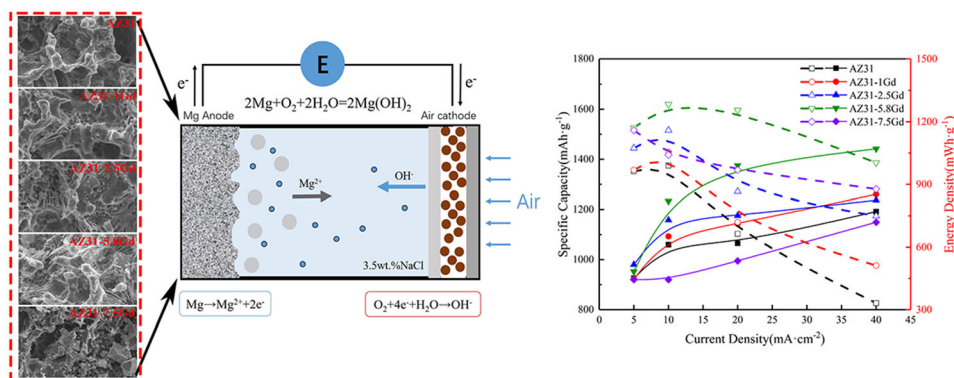
In this research, cast magnesium alloys AZ31-xGd are assessed as anode material candidates for primary Mg-air batteries. The effects of Gd content in the microstructure, discharge behavior and electrochemical properties of cast AZ31 as an anode are studied through microstructure characterization, electrochemical measurements and battery discharge tests. Results indicate that the introduction of Gd can refine α -Mg grains. The discharge and electrochemical properties of magnesium alloys are improved by optimizing its composition. We confirm that the Al₂Gd can restrain the kinetics of hydrogen evolution reaction. The acicular structure can connect the magnesium alloy matrix and reduce the chunk spalling. The data suggest that AZ31-5.8Gd alloy has the best self-corrosion resistance performance and discharge behavior among all prepared AZ31-xGd alloys. AZ31-5.8Gd can output a high specific capacity of 1411.8 mAh g⁻¹ and a high energy density of 1153 mWh g⁻¹ at the current density of 40 mA cm⁻². The anode efficiency can reach up to 63.21%. The addition of Gd properly can optimize magnesium alloy microstructure and improve the discharge performance.

Handling Editor: Catalin Croitoru.

Address correspondence to E-mail: upcxiongwei@163.com

<https://doi.org/10.1007/s10853-021-06135-2>

GRAPHICAL ABSTRACT



Introduction

The increasing demands for energy and serious environmental pollution have promoted the development of green and sustainable energy such as hydropower, solar power, wind power and marine energy [1, 2]. However, the popularization of green energy is limited by its instability, unpredictability and intermittency [3, 4]. The key to sufficient use of renewable energy is efficient energy storage and conversion technology, such as battery technology [5]. Up to now, mobile electronic equipment, large-scale energy storage and electric vehicles have benefited from the improvement of battery technology due to its effective storage and power conversion capabilities [6–8]

In recent years, battery technology with low cost and high energy density has become a research focus on practical storage and use of renewable energy [4].

The current dominance of lithium-ion batteries in the market is mainly because of their high specific capacity, long service life and lightweight structure design [9, 10].

Since there are highly requirements in storing and transforming energy as well as electrical transportation, the specific capacity and power density of lithium-ion battery technology need to be advanced. However, limited by the restriction of its theoretical specific capacity and structural design, traditional lithium-ion battery technology is approaching to its theoretical ceiling [11–13]. At the same time, lithium-ion battery technology is also limited by high manufacturing costs, and other battery technologies are booming. In the future, battery technology is not a post-lithium era, but a coexistence era of multiple batteries [14].

The fuel cell is an ideal energy conversion way due to its high energy conversion rate and environmental friendliness [15]. Metal-air battery has become a

Table 1 Parameters and reactions of various metal-air batteries

Batteries	Voltage (V)	Theoretical energy density (mWh g ⁻¹)	Theoretical specific capacity (mAh g ⁻¹)	Price (\$ kg ⁻¹)	Reaction
Mg-air	3.09	6901	2233	2.476	$2\text{Mg} + \text{O}_2 + 2\text{H}_2\text{O} \rightarrow 2\text{Mg}(\text{OH})_2$
Al-air	2.71	8070	2978	2.656	$4\text{Al} + 3\text{O}_2 + 6\text{H}_2\text{O} \rightarrow 4\text{Al}(\text{OH})_3$
Li-air	2.96	11,497	3884	89.144	$2\text{Li} + \text{O}_2 \rightarrow \text{Li}_2\text{O}_2$
Zn-air	1.65	1360	825	3.334	$2\text{Zn} + \text{O}_2 \rightarrow 2\text{ZnO}$
Na-air	2.33	2715	1165	3.200	$2\text{Na} + \text{O}_2 \rightarrow \text{Na}_2\text{O}_2$
K-air	2.48	1704	687	17.524	$\text{K} + \text{O}_2 \rightarrow \text{KO}_2$

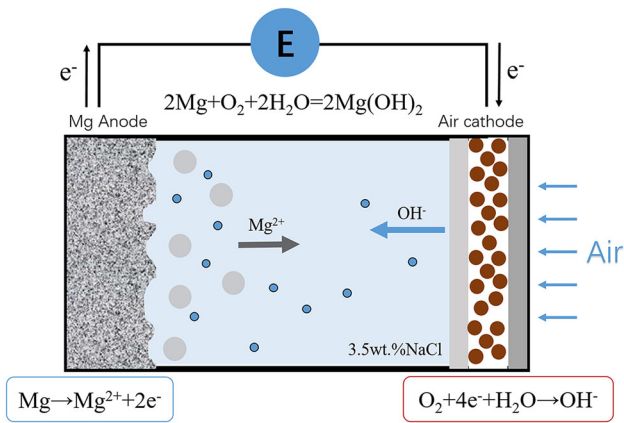


Figure 1 The structure and working principle of Mg-air battery.

research hotspot due to the specific capacity much higher than traditional lithium-ion batteries because of the unique semi-open structure [16]. Table 1 shows the current parameters and reactions of most metal-air batteries. Although lithium-air batteries have higher discharge performance, lithium metal is not widely used due to its high price and scarce supply. The aluminum air battery also has good discharge performance, but the dense passivation film on the surface of the metal aluminum will hinder the discharge of the aluminum electrode. The magnesium-air battery has attracted attention because of high theoretical specific capacity, high energy density and low manufacturing cost [17–20]. Magnesium anode is a desired anode material for its low standard electrode potential (−2.37 V vs. SHE) and high theoretical energy density (6800 mWh g^{−1}) [21–23]. Figure 1 shows the schematic diagram of magnesium-air battery. The anode material is pure magnesium or magnesium alloy, the electrolyte solution is NaCl solution, and the oxygen in the air serves as the cathode [24]. The self-corrosion of hydrogen evolution caused by the negative differential effect will reduce the anode efficiency of magnesium-air battery and reduce the battery life [25, 26]. In addition, factors such as slow cathode redox reaction kinetics, anode polarization and discharge products accumulation can lead to lower battery voltages [27–31].

To make magnesium anode material reach the required level for power applications, it is crucial to find a way to improve the discharge performance [32]. Some studies have shown that alloying can adjust the microstructure of magnesium alloy, enhance the corrosion resistance under open circuit potential, activate its discharge and improve the

continuous discharge capability by strengthening the discharge products spalling [33–35]. Gd is widely used in the modification of magnesium alloys due to its special atomic structure. However, most researchers mainly study the effect of Gd on the mechanical properties of magnesium alloys [36–38]. Recently, Liu reported the positive effect of Al₂Gd particles in extruded magnesium alloy on anodic discharge [39]. Chen et al. have reported the effect of rare earth elements La and Gd in cast AZ80-La-Gd magnesium alloy and LPSO structure in Mg_{95.28}-Gd_{3.72}Zn_{1.00} after heat treatment on discharge and electrochemical properties [40, 41]. However, the effects of as-cast alloy and Gd content on the performance of air anode are rarely reported. It is meaningful to research the effect of the introduction of Gd on the shape and distribution of the second phase in cast magnesium alloys as well as the influence of the microstructure on the discharge performance.

In this research, AZ31-*x*Gd (*x* = 0, 1, 2.5, 5.8, 7.5) were prepared. The above magnesium alloys are applied to assemble magnesium-air batteries. The microstructure and properties of cast magnesium alloys with different Gd contents were studied. The goal of this paper is to explore the effect of Gd content on the microstructure of cast AZ31 magnesium alloy and discuss the relationship between microstructure and discharge properties. This work also aims to test the reliability of the optimized cast AZ31-Gd magnesium alloy as an anode and provide a new thought for the development of high specific capacity and high energy density magnesium-based alloy anode materials for Mg-air batteries.

Table 2 Chemical composition of experimental alloys (wt.%)

Alloys	Al	Zn	Mn	Si	Ce	Mg
AZ31	2.834	1.118	0.354	0.147	0	Bal
AZ31-1Gd	2.852	1.135	0.310	0.124	0.845	Bal
AZ31-2.5Gd	2.716	1.004	0.357	0.151	1.995	Bal
AZ31-5.8Gd	2.637	1.006	0.292	0.179	4.654	Bal
AZ31-7.5Gd	2.650	1.088	0.236	0.099	6.376	Bal

Experimental

Preparation of alloys

Five types of magnesium alloy anodes were made by commercially available AZ31 magnesium alloy (Mg-3.1Al-0.82Zn-0.33Mn), pure aluminum (99.90%), pure zinc (99.995%) and Mg-25Gd alloy as raw materials. AZ31 magnesium alloy was melted in a mild steel crucible by heating in a resistance furnace to 740 °C. Then the magnesium gadolinium alloy, pure aluminum and pure zinc were added. After 15 min of heat preservation, the mixed melt was heated to 780 °C. Then the mixture is refined, scraped, stirred, cooled to 720 °C rapidly and poured into the graphite mold preheated to 200 °C. The above steps were carried out in the atmosphere of CO₂ + SF₆. Finally, the cast magnesium alloy is cooled at room temperature. The size of the columnar ingot is $\Phi 28 \times 165$ mm. The samples for analysis were cut from the cast magnesium alloys by CNC EDM wire-cutting machines. The composition of cast Mg alloy was analyzed by the X-ray fluorescence analyzer (PANalytical). The composition of the magnesium alloy is listed in Table 2.

Microstructure characterization

The microstructure samples were sanded by various specifications of SiC sandpapers, then polished with diamond paste and ethyl alcohol. Finally, the surface was etched by a solution of nitric acid and alcohol. The microstructure observation was implemented with the optical microscopy (OLYMPUS). The phase composition was analyzed by the X-ray diffraction (XRD, PANalytical X'Pert PRO MPD). The phase morphology and distribution were observed by the field emission scanning electron microscope (FE-SEM, JEOL JSM-7200F) coupled with energy-dispersive spectrometer (EDS, Oxford Max50).

Mg-air battery performance test

The capacity of anode was studied by using a simple assembly cell model. The anode was magnesium alloy for research. The catalyst for the air cathode was MnO₂, and the current collector was nickel mesh. The distance between magnesium alloy anode and air cathode was 14 mm, and the reaction area of air cathode and magnesium-based alloy anode was 1

cm². And the electrolyte solution between the anode and cathode was 5 ml of 3.5 wt.% NaCl solution. The battery performance of magnesium-air battery at different current densities was tested with a constant current discharge system. The test time was 3 h, and the current densities were, respectively, 5, 10, 20 and 40 mA cm⁻². After the discharge process, the magnesium alloy anode sample was cleaned with boiling chromium trioxide solution (200 g L⁻¹). And the discharged surface topography was studied by the scanning electron microscopy. The actual anode efficiency and specific capacity of the studied anodes were obtained by mass loss method.

Electrochemical measurements

Magnesium alloy samples for electrochemical tests were ground by the 2000 grit SiC paper and tested on CORRTEST CS350H electrochemical workstation. The test was conducted by a conventional three-electrode method. The working electrodes were magnesium alloys to be tested, and the exposure area is 1 cm². A platinum net with an area of 15 × 20 was used as the counter electrode. The SCE was used as a reference electrode. The electrolyte was a NaCl solution with a concentration of 3.5 wt.% and a volume of 250 mL. All measurements were maintained at 298 ± 5 K. When the electrochemical samples

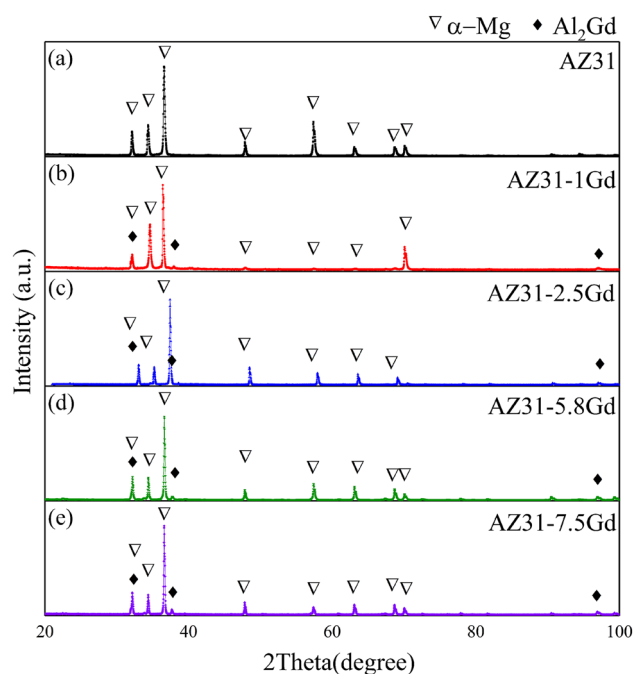
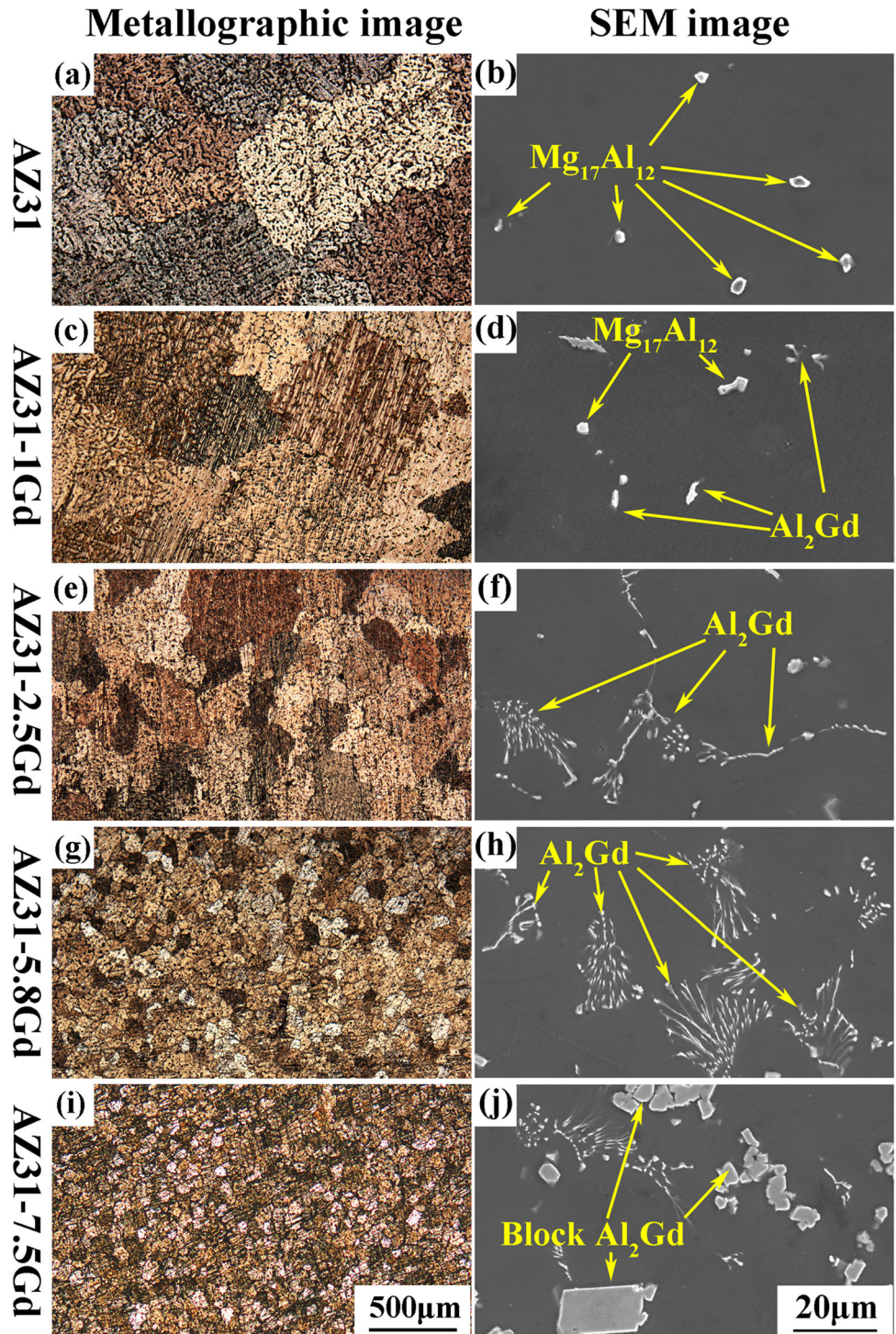


Figure 2 XRD patterns of the researched Mg anodes.

Figure 3 Microstructures of the Mg alloy anodes.



reached a stable state through soaking in the electrolyte for 5 min, the electrochemical impedance spectroscopy (EIS) was began. During the EIS analysis, the scanning frequency was set from 100,000 Hz to 0.01 Hz with a 10 mV driving voltage. From -0.5 V to $+0.5$ V (vs. OCR), the potentiodynamic

polarization curves were tested and the scan rate was $0.3333 \text{ mV}\cdot\text{s}^{-1}$.

Results and discussion

Microstructure

Figure 2 shows the XRD pattern of prepared magnesium alloy anode. The main phase of AZ31 magnesium alloy is α -Mg. There are no β peaks in the XRD curve of AZ31 magnesium alloy. It is caused by the low β content. The introduction of Gd produces the second phase of Al_2Gd . The electronegativity difference between Gd and Al is relatively large, and Al_2Gd has a higher melting point. It is the first to precipitate during the casting and solidification of the alloy, and the content is higher. With the increase in addition Gd element, the characteristic peak of Al_2Gd increases, indicating that the content of Al_2Gd increases accordingly.

Figure 3 shows the metallographic and scanning electron micrographs of five researched magnesium alloys. The grains are coarse on AZ31 magnesium alloy (Fig. 3a). A small amount of phase β is distributed on the α magnesium matrix (Fig. 3b). The volume of Al_2Gd particles increases and the volume of $\text{Mg}_{17}\text{Al}_{12}$ particles decreases by introducing the Gd

element in AZ31 magnesium alloy. For example, when the Gd element content is 1 wt.%, the second phase is part of $\text{Mg}_{17}\text{Al}_{12}$ phase and Al_2Gd phase (Fig. 3d). When the Gd element content is 2.5 wt.%, the $\text{Mg}_{17}\text{Al}_{12}$ phase disappears, and the second phase is Al_2Gd , which is acicular and concentrated (Fig. 3f). When the addition of Gd is 5.8 wt.%, the acicular Al_2Gd aggregates into clusters (Fig. 3h). And the introduction of Gd can refine the grains of the magnesium alloy (Fig. 3c). With the increase in the content of Gd, the degree of grain refinement becomes more obvious (Fig. 3e). The degree of grain refinement has reached a high level while the Gd content reaches 5.8 wt.% (Fig. 3g). And with the continuous addition of Gd, the crystal grains will still be refined, but the trend is no longer obvious (Fig. 3i), and the volume fraction of acicular Al_2Gd decreases, and there will be massive Al_2Gd precipitation when the addition is 7.5 wt.% (Fig. 3j). With the introduction of Gd element, the number of β phase is reduced, and a new second phase is precipitated at the grain boundary. The newly generated phase is Al_2Gd , which is proved by EDS composition analysis and XRD phase analysis. This is because the

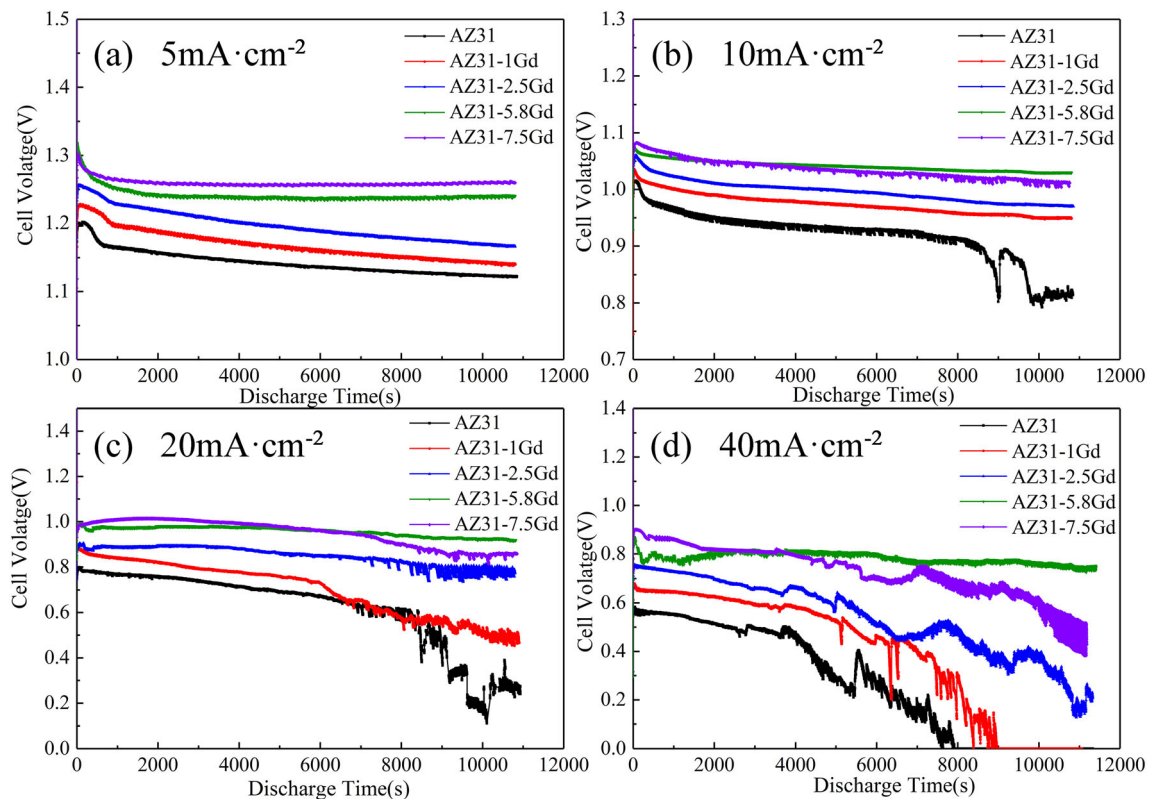


Figure 4 Discharge voltage of the investigated Mg-based anodes for Mg-air batteries in 3.5 wt.% NaCl solution.

electronegativity disparity between Gd and Al is larger than that of Mg and Al, which causes Al_2Gd to precipitate first during the solidification of the alloy.

Mg-air battery performance

In Fig. 4, the constant current discharge performance of studied magnesium alloy anodes for magnesium-air battery was studied at current densities of 5, 10, 20 and 40 $mA\ cm^{-2}$. For instance, the Fig. 4a shows that the discharge current density is 5 $mA\ cm^{-2}$. In the first 1000 s of discharge test, the initial voltage is $AZ31 < AZ31-1Gd < AZ31-2.5Gd < AZ31-5.8Gd < AZ31-7.5Gd$. It can be inferred that the Gd addition would boost the discharge voltage of magnesium alloy. It is noteworthy that the voltage drops extremely fast during the first 1000 s of the discharge process. The reason is that the surface morphology changes rapidly at the beginning of discharge behavior. The rate of discharge product shedding is lower than a generation, resulting in a reduction active material, which makes discharge voltage decrease. The formation and shedding of discharge products are balanced, and the rate of discharge voltage decrease slows down with the reaction. The introduction of Gd can optimize the voltage reduction at the initial stage of magnesium anode discharge and improve the discharge stability of magnesium alloy anode.

The discharge current density is 10 $mA\cdot cm^{-2}$ which is shown in Fig. 4b. The voltage at the beginning of the discharge phase increases with the Gd content increasing, and AZ31 magnesium alloy

exhibits an unstable and large decrease during discharge reaction. This phenomenon is alleviated with the addition of Gd. For example, the voltage decrease and fluctuation are the smallest when the Gd content is 5.8 wt.%. While the AZ31-7.5Gd also has a higher discharge voltage, which almost coincides with AZ31-5.8Gd, there is a small amount of fluctuation, which may be caused by uneven peeling of the block second phase. Figure 4c shows the voltage changes of five investigated magnesium alloy anodes while the current density is 20 $mA\ cm^{-2}$. The discharge voltage of AZ31 magnesium alloy shows a significantly fluctuating state after the discharge time exceeds 7000 s, and the voltage drops considerably. The voltage fluctuation decreases after introducing Gd element, and with the increase of it, the voltage drop of magnesium alloy anode decreases. The discharge voltage of five researched magnesium alloy anodes become very unstable until the current density is 40 $mA\ cm^{-2}$ (Fig. 4d). For example, AZ31 and AZ31-1Gd magnesium alloys terminate the discharge reaction after voltage drops to 0 V after 8000 and 9078 s. After a long-term discharge, the discharge voltage of AZ31-2.5Gd also becomes unstable and decreases greatly. The anode discharge performance of magnesium alloy tends to be stable when the Gd content continues to increase. The discharge potential of AZ31-5.8Gd is the most stable among five magnesium alloys. On the contrary, the voltage potential of AZ31-7.5Gd with higher Gd content becomes wider after 6000 s of discharge. The phenomenon indicates that the discharge voltage fluctuates significantly in a short time and the surface of AZ31-7.5Gd magnesium alloy anode changes remarkable after long-term discharge. The discharge products fall off unevenly. Through the above analysis, the proper addition of Gd will improve the discharge stability of magnesium alloy anode, especially in a high current density, and the discharge voltage is the most stable when the Gd content is 5.8 wt.%.

Figure 5 shows the specific capacity and energy density of five researched anodes at different ampere densities. Table 3 shows the anodic efficiency. The specific capacity of five researched electrodes at low current density is not much different. The actual specific capacity is 980.39 $mAh\ g^{-1}$ for AZ31-2.5Gd, and the lowest is 920.25 $mAh\ g^{-1}$ for AZ31-7.5Gd (theoretical specific capacities are 2198.67 and 2112.43 $mAh\ g^{-1}$ separately). The anode efficiency of them is 43.896 and 41.203%. The enhancement of the

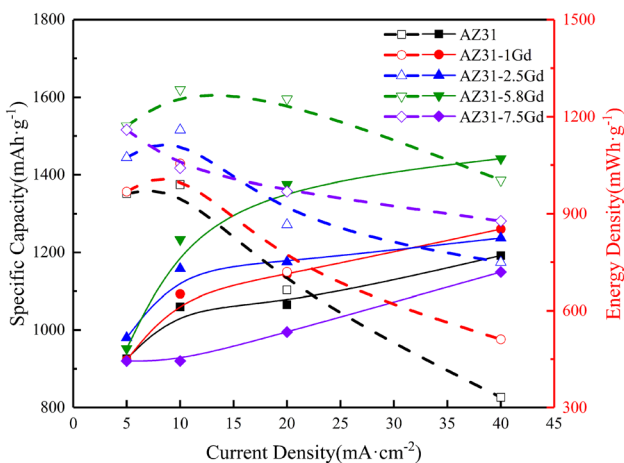
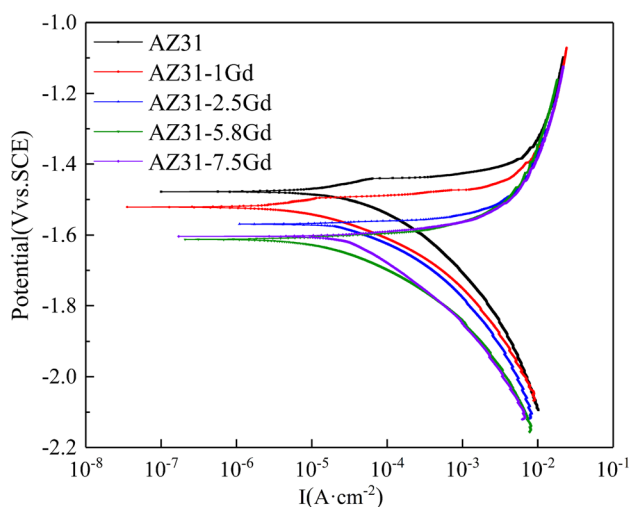


Figure 5 Specific capacity and energy density of the five researched Mg anodes.

Table 3 The anodic efficiency

Magnesium alloys	5 mA cm ⁻²	10 mA cm ⁻²	20 mA cm ⁻²	40 mA cm ⁻²
AZ31	41.457%	47.463%	47.772%	53.372%
AZ31-1Gd	41.331%	48.940%	51.189%	56.438%
AZ31-2.5Gd	43.896%	51.862%	52.649%	55.399%
AZ31-5.8Gd	42.631%	55.221%	61.573%	63.210%
AZ31-7.5Gd	41.203%	41.205%	44.552%	51.464%

**Figure 6** Polarization curves of AZ31, AZ31-1Gd, AZ31-2.5Gd, AZ31-5.8Gd and AZ31-7.5Gd alloy in 3.5 wt.% NaCl solution.

discharge current density is beneficial to the specific capacity of anode [42]. So the specific capacity of research electrode is also increasing with the enhancement of the current density. It is worth noting that at high current densities, such as 20–40 Ma cm⁻², the increase in specific capacity begins to slow down. It is also shown in the figure that the energy density of five magnesium alloy anodes increases firstly and then decreases. The energy density reaches the highest value at 10 mA cm⁻². The AZ31-5.8Gd magnesium alloy owns the highest energy density, which can reach 1284 mWh g⁻¹. The energy density is accompanied with the continuous rising of current density. The energy density of AZ31-5.8Gd is still the highest when the current density reaches 40 mA cm⁻², and it can maintain at 89.9% of the peak energy density. At this time, the anode efficiency can reach

63.210%. From the above analysis, the specific energy increase is no longer significant under high current density, but the energy density will decrease. Considering the trend of specific energy and energy density comprehensively, AZ31-5.8Gd magnesium alloy is an anode and enjoys promising future in air batteries.

Electrochemical performance

Figure 6 shows the potentiometric scanning curve of five research electrodes in 3.5 wt.% NaCl solution. The AZ31 magnesium alloy has the highest positive corrosion potential. The corrosion potential decreases after the introduction of Gd. The cathodic hydrogen evolution reaction (HER) kinetics decreases with the increase in Gd addition. The Tafel slope of AZ31 magnesium alloy and AZ31-1Gd magnesium alloy have an obvious transition at the anode end of the polarization curve. The transition of AZ31-1Gd magnesium alloy is smaller than that of AZ31 magnesium alloy. As the Gd increases continuously, the Tafel anode branch slope of Tafel polarization curve of magnesium alloy will not change suddenly. This transition point shows a protective surface film forms on the surface of magnesium alloy. When potential exceeds this transition point, the surface film ruptures and the corrosion current density increases sharply [43]. The introduction of Gd can inhibit formation of magnesium alloy surface film and improve the anode activity. Table 4 shows the calculation of corrosion parameters of magnesium alloys in 3.5 wt.% NaCl solution by the cathode Tafel extrapolation method. Due to the negative difference effect (NDE), the slope of the anode branch of the Tafel

Table 4 Corrosion parameters of AZ31, AZ31-1Gd, AZ31-2.5Gd, AZ31-5.8Gd and AZ31-7.5Gd alloy in 3.5 wt.% NaCl solution from polarization curves

Magnesium alloys	AZ31	AZ31-1Gd	AZ31-2.5Gd	AZ31-5.8Gd	AZ31-7.5Gd
B _c /mV	-124.63	-109.32	-96.197	-86.81	-129.1
J _{corr} /A·cm ⁻²	3.2262E-5	2.8313E-5	2.5963E-5	1.1935E-5	2.6397E-5
E _{corr} (vs. SCE)/V	-1.4782	-1.5170	-1.5851	-1.6183	-1.6095

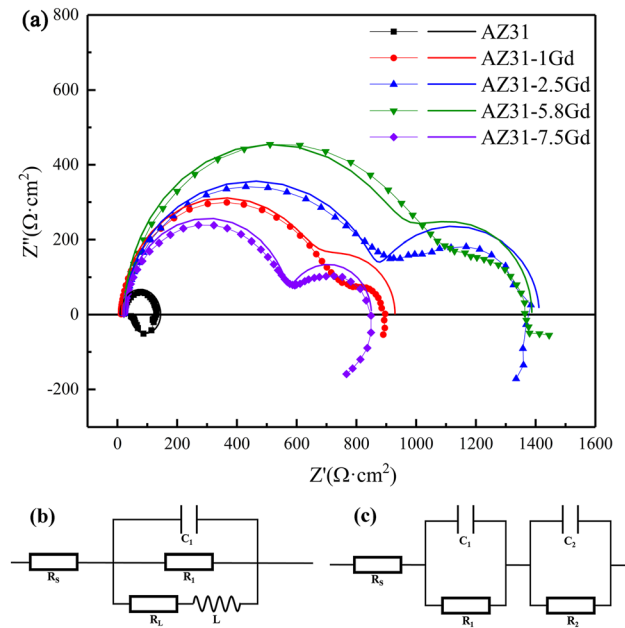


Figure 7 a EIS patterns and fitting curves of AZ31, AZ31-1Gd, AZ31-2.5Gd, AZ31-5.8Gd and AZ31-7.5Gd alloy in 3.5 wt.% NaCl solutions. (b) Equivalent circuit of EIS of pure AZ31 alloy in 3.5 wt.% NaCl solutions. (c) Equivalent circuit of EIS of AZ31-1Gd, AZ31-2.5Gd, AZ31-5.8Gd and AZ31-7.5Gd alloys in 3.5 wt.% NaCl solutions.

polarization curve does not have a good current relationship, so the fitting calculation is carried out through the cathode branch of the Tafel polarization curve [44]. The smallest corrosion current density is AZ31-5.8Gd magnesium alloy. It shows that AZ31-5.8Gd has better corrosion resistance at open circuit potential. In the anode branch, the introduction of Gd element can increase the corrosion current density of magnesium alloys. At the same time, AZ31-5.8Gd can be obtained by Table 3 with higher anode efficiency. It can be concluded that the introduction of Gd element can reduce the parasitic corrosion phenomenon of magnesium anode. In summary, AZ31-5.8Gd has

good electrochemical activity and high anode efficiency due to the introduction of Gd element.

The EIS curves of samples are shown in Fig. 7a. The EIS curves of different magnesium alloys have a loop in the low-frequency region and high-frequency region, respectively. The EIS curve of AZ31 magnesium alloy is different in the high- and low-frequency regions, which is a capacitive semicircle and an inductive semicircle separately. There is a capacitive reactance semicircle in the high-frequency and low-frequency regions after introducing Gd element. The appearance of AZ31 magnesium alloy inductive semicircle is due to the intermediate product of electrode reaction. This intermediate product is adsorbed on electrode surface to produce the adsorption complex. Figure 7b is an equivalent circuit model which is the simulation of this process. The state of electrode surface changed after the introduction of Gd. The curve of high-frequency region is connected to the oxide film on the surface of AZ31 magnesium alloy, while the curve of middle frequency region is connected to the charge transfer process [45]. The adsorptive substance produced by the electrode reaction is precipitated on the electrode surface and covered on the compact electric double layer, which has a certain capacitive impedance. The corrosion product film is connected with the electric double layer in series to form an impedance spectrum with two time constants. The first capacitive semicircle of magnesium alloy anode is significantly increased after the introduction of Gd element, which explains that the introduction of Gd can effectively enhance corrosion resistance of magnesium alloys. While the Gd addition is 5.8 wt.%, the capacitive semicircle radius is the largest, indicating that the alloy possesses the best corrosion resistance. The results are in good agreement with the polarization curve analysis. Figure 7c shows an equivalent circuit model which is the simulation of this process.

Table 5 EIS simulated values of AZ31, AZ31-1Gd, AZ31-2.5Gd, AZ31-5.8Gd and AZ31-7.5Gd alloy in 3.5 wt.% NaCl solution

Magnesium alloys	AZ31	AZ31-1Gd	AZ31-2.5Gd	AZ31-5.8Gd	AZ31-7.5Gd
R_s/Ω	2.206E1	2.304E1	2.305E1	2.259E1	2.260E1
C_1/F	1.520E-5	8.528E-6	8.925E-6	7.787E-6	9.969E-6
R_1/Ω	1.087E2	8.322E2	7.585E2	8.534E2	5.170E2
L/H	2.533E2	–	–	–	–
R_L/Ω	3.882E1	–	–	–	–
C_2/F	–	8.9279E-6	7.860E-5	2.269E-4	1.756E-3
R_2/Ω	–	2.462E3	4.085E2	4.296E2	2.435E2

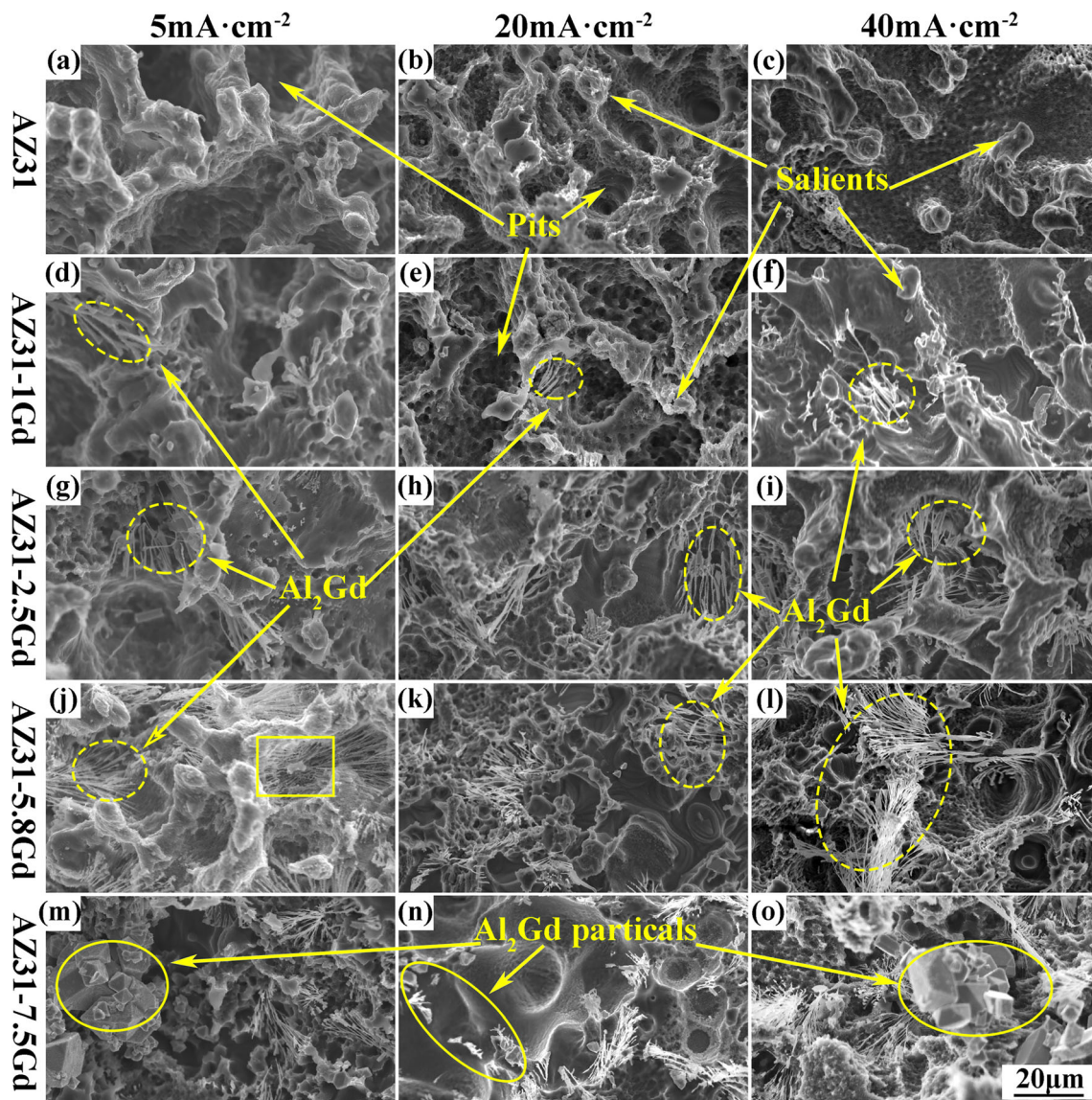


Figure 8 The surface morphologies of magnesium-based anodes after discharge at different current densities.

Table 5 reveals the simulated EIS values of five researched magnesium alloys in 3.5 wt.% NaCl solution, where R_s represents solution resistance, C_1 represents electric double layer capacitance, R_1 represents charge transfer resistance, L and R_L , respectively, represent the adsorption and decomposition process of the intermediate formed on the electrode surface, C_2 and R_2 , respectively, represent the capacitive reactance and resistance of the adsorbent material covering the electrode surface produced by the electrode reaction. Generally, the exchange current is directly contented with the electrochemical process of corrosion [46]. The introduction of Gd content can enhance the corrosion resistance. The

capacitive reactance C_2 of adsorption film on the electrode surface of electrode reaction product improves with the increase in the amount of Gd added. The thickness of the adsorption film increases with Gd addition. High R_2 indicates the high corrosion resistance and low dissolution rate [47]. When the Gd content is 5.8 wt.%, magnesium alloy has the best corrosion resistance. Under the open circuit, Gd can effectively make the electrode reaction product adhere to electrode surface, reduce the dispersion effect of electrode in electrolyte and improve its corrosion resistance.

Electrode surface analysis after discharge

Figure 8 is the SEM photographs of five kinds of magnesium alloys to study the discharge morphology under different current densities. Figure 8a, b shows that the surfaces of AZ31 magnesium alloy anode react locally at low current density, producing pits and bumps. Their presence increases the contact area between anode surface and electrolyte. However, the actual specific capacity and anode efficiency are much lower than the theoretical value due to the well-known negative difference effect [25]. Reasons for the decrease in anode efficiency are the self-corrosion of hydrogen evolution of magnesium alloy and the thin bonding part between protruding part and substrate, which is easy to break and fall off at the root. As the current density increases, the area and depth of pits become smaller, and the convex particles also decrease. When the current density reaches $40 \text{ mA}\cdot\text{cm}^{-2}$, the anode surface is flat (Fig. 8c). The low discharge current density makes anode self-corrosion phenomenon severe. Increasing discharge current density can reduce the unevenness of surface, reduce anode reaction area, reduce discharge voltage and increase power density slowly. However, the phenomenon of particle shedding on the surface of magnesium anode is alleviated to a certain extent, and the efficiency of magnesium anode is improved. Combining the discharge performance with a voltage of 0 V after severe fluctuations, it can be inferred that the discharge product of AZ31 magnesium alloy will cover the surface of anode and terminate discharge reaction when the current density is 40 mA cm^{-2} . With the introduction of Gd, acicular Al_2Gd phase formed by combination of Al and Gd is distributed on $\alpha\text{-Mg}$ matrix. The content of Al_2Gd is very small when Gd addition is 1 wt.%, and there are still more pits and bumps at low current density (Fig. 8d). The acicular Al_2Gd phase will connect protrusions produced on $\alpha\text{-Mg}$ matrix during discharge reaction. The protrusions produced on $\alpha\text{-Mg}$ matrix are connected (Fig. 8e). Acicular Al_2Gd phase may penetrate through $\alpha\text{-Mg}$ matrix (Fig. 8f). The number of Al_2Gd increases when Gd addition reaches 2.5 wt.%. The reduction of bumps indicates that Al_2Gd can effectively suppress the occurrence of uneven local reactions at low current densities (Fig. 8g). It can be observed from Fig. 8h, i that anode surface is relatively flat, which suggests that Al_2Gd can promote the discharge reaction

process of magnesium anode to proceed uniformly. When the amount of Gd added reaches 5.8 wt.%, some bumps can still be seen under low current density. But because the acicular Al_2Gd is connected, the bumps are not easy to fall off, and the chunk spelling is reduced (Fig. 8j). Since the electrode potential of Al_2Gd is slightly higher than that of $\alpha\text{-Mg}$ [48, 49], the evenly distributed Al_2Gd can accelerate the consumption of convex part and promote the uniform reaction of anode without forming large hydrogen evolution self-corrosion. It is worth noting that only a small amount of Al_2Gd is observed in Fig. 8k. The reason is that the discharging product generated during discharge reaction will adhere to acicular Al_2Gd and fall off with Al_2Gd , so that the discharge reaction is sustainable. When the Gd addition continues to increase to 7.5 wt.%, Al_2Gd precipitates as a massive second phase as can be observed in in Fig. 8m, n, o. The agglomerated bulk Al_2Gd not only fails to promote the uniform discharge of Mg matrix, but also falls off from the matrix easily, making the chunk spelling severer. It does not contribute to the specific capacity of magnesium alloy anode and reduces the anode efficiency of magnesium alloy anode.

The dispersed and uniformly distributed Al_2Gd second phase not only provides protection for the surface of magnesium alloy anode, but can also promotes the uniform consumption of $\alpha\text{-Mg}$ matrix around Al_2Gd . The acicular second phase can also adsorb discharge reaction products, accumulate the discharge products and promote the shedding of discharge products on anode surface, so that the discharge reaction can proceed uniformly and lastingly. Therefore, the discharge performance of magnesium alloy anode containing acicular Al_2Gd phase is better than that of AZ31 magnesium alloy, which has certain guidance for the further research of magnesium-based alloy anode.

Conclusion

This work has studied in detail the as-cast AZ31-xGd magnesium alloy anode for magnesium-air batteries and the effect of Gd addition on the discharge and electrochemical properties of cast magnesium alloy anode. Compared with AZ31 magnesium alloy, the AZ31-Gd magnesium alloy anode has better discharge performance, and the discharge performance

is best when the addition amount of Gd reaches 5.8 wt.%. AZ31-5.8Gd can output a high energy density of 1284 mWh g⁻¹ and a high specific capacity of 1411.8 mAh g⁻¹ at a current density of 10 mA cm⁻². The excellent performance of AZ31-5.8Gd magnesium alloy anode should be attributed to the acicular Al₂Gd uniformly distributed on α-Mg matrix. The presence of them can inhibit the kinetics of hydrogen evolution reaction. The special acicular structure can reduce the loss of anode efficiency caused by partial loss of uneven local consumption. The evenly distributed Al₂Gd promotes the dissolution of α-Mg matrix uniformly and accelerates shedding of discharge products, so that the voltage is maintained in a stable state. When the current density exceeds 10 mA cm⁻², the specific capacity and energy density of AZ31-5.8Gd exceed other four researched magnesium alloys. The addition of a proper amount of Gd can effectively optimize magnesium alloy microstructure, perfect discharge reaction process and increase its capacity at high current density.

Acknowledgements

The authors gratefully acknowledge the support from the Natural Science Foundation of Shandong Province of China (ZR2019MEM020, ZR2019MEE108 and ZR2017LEM004) and Fundamental Research Funds for the Central Universities (18CX05002A and 19CX05001A).

References

- [1] Fu YH, Zhao H, Piao SL, Peaucelle M, Peng SS, Zhou GY, Ciais P, Huang MT, Menzel A, Uelas JP, Song Y, Vitasse Y, Zeng ZZ, Janssens IA (2015) Declining global warming effects on the phenology of spring leaf unfolding. *Nature* 526:104–107. <https://doi.org/10.1038/nature15402>
- [2] Lesk C, Rowhani P, Ramankutty N (2016) Influence of extreme weather disasters on global crop production. *Nature* 529:84. <https://doi.org/10.1038/nature16467>
- [3] Chu S, Cui Y, Liu N (2016) The path towards sustainable energy. *Nat Mater* 16:16–22. <https://doi.org/10.1038/nmat4834>
- [4] Chu S, Majumdar A (2012) Opportunities and challenges for a sustainable energy future. *Nature* 488:294–303. <https://doi.org/10.1038/nature11475>
- [5] Schmuck R, Wagner R, Horpel G, Placke T, Winter M (2018) Performance and cost of materials for lithium-based rechargeable automotive batteries. *Nat Energy* 3:267–278. <https://doi.org/10.1038/s41560-018-0107-2>
- [6] Kwade A, Haselrieder W, Leithoff R, Modlinger A, Dietrich F, Droeder K (2018) Current status and challenges for automotive battery production technologies. *Nat Energy* 3:290–300. <https://doi.org/10.1038/s41560-018-0130-3>
- [7] Liu C, Feng L, Ma LP, Cheng HM (2010) Advanced materials for energy storage. *Adv Mater* 22:E28–E62. <https://doi.org/10.1002/adma.200903328>
- [8] Yang Z, Zhang J, Kintner-Meyer MCW, Lu X, Choi D, Lemmon JP, Liu J (2011) Electrochemical energy storage for green grid. *Chem Rev* 111:3577–3613. <https://doi.org/10.1021/cr100290v>
- [9] Zhang X, Wang XG, Xie Z, Zhou Z (2016) Recent progress in rechargeable alkali metal-air batteries. *Green Energy Environ* 1:4–17. <https://doi.org/10.1016/j.gee.2016.04.004>
- [10] Choi JW, Aurbach D (2016) Promise and reality of post-lithium-ion batteries with high energy densities. *Nat Rev Mater* 1:16013. <https://doi.org/10.1016/j.gee.2016.04.004>
- [11] Lu J, Chen Z, Ma Z, Feng P, Amine K (2017) The role of nanotechnology in the development of battery materials for electric vehicles. *Nat Nanotechnol* 12:1031–1038. <https://doi.org/10.1038/nnano.2016.292>
- [12] Michael M, Thackeray CW, Eric D, Isaacs, (2012) Electrical energy storage for transportation—approaching the limits of, and going beyond, lithium-ion batteries. *Energy Environ Sci* 5:7854–7863. <https://doi.org/10.1039/c2ee21892e>
- [13] Ko M, Chae S, Ma J, Kim N, Lee HW, Cui Y, Cho J (2016) Scalable synthesis of silicon-nanolayer-embedded graphite for high-energy lithium-ion batteries. *Nat Energy* 1:16113. <https://doi.org/10.1038/nenergy.2016.113>
- [14] Durmus YE, Zhang H, Baakes F, Desmaizieres G, Hayun H, Yang L, Kolek M, Küpers V, Janek J, Mandler D (2020) Side by side battery technologies with lithium on based batteries. *Adv Energy Mater* 10:2000089. <https://doi.org/10.1002/aenm.202000089>
- [15] Shin MH, Eom TH, Park YH, Won CY (2016) Design and control of fuel cell-battery hybrid system for forklift. In: 2016 IEEE transportation electrification conference and expo, Asia-Pacific (ITEC Asia-Pacific), pp 584–589. <https://doi.org/10.1109/ITEC-AP.2016.7513020>
- [16] Li YG, Lu J (2017) Metal-air batteries: will they be the future electrochemical energy storage device of choice? *Acs Energy Lett* 6:1370–1377. [https://doi.org/10.1021/acsenergylett.7b00119](https://doi.org/10.1021/acseenergylett.7b00119)
- [17] Lee JS, Kim S, Cao R, Choi NS, Liu M, Lee KT, Cho J (2011) Metal-air batteries with high energy density: Li-air

- versus Zn-air. *Adv Energy Mater* 1:34–50. <https://doi.org/10.1002/aenm.201000010>
- [18] Liu X, Xue J, Zhang D (2019) Electrochemical behaviors and discharge performance of the as-extruded Mg-1.5 wt% Ca alloys as anode for Mg-air battery. *J Alloy Compd* 790:822–828. <https://doi.org/10.1016/j.jallcom.2019.03.260>
- [19] Xu NN, Nie Q, Luo LYQ, Yao CZ, Gong QJ, Liu YY, Zhou XD, Qiao JL (2019) Controllable hortensia-like MnO₂ synergized with carbon nanotubes as an efficient electrocatalyst for long-term metal-air batteries. *ACS Appl Mater Inter* 11:578–587. <https://doi.org/10.1021/acsami.8b15047>
- [20] Li X, Lu H, Yuan S, Bai J, Wang J, Cao Y, Hong Q (2017) Performance of Mg-9Al-1In alloy as anodes for mg-air batteries in 3.5 wt% NaCl solutions. *J Electrochem Soc* 164:A3131–A3137. <https://doi.org/10.1149/2.0971713jes>
- [21] Xiong H, Zhu H, Luo J, Yu K, Shi C, Fang H, Zhang Y (2020) Effects of heat treatment on the discharge behavior of Mg-6wt%Al-1wt%Sn alloy as anode for magnesium-air batteries. *J Mater Eng Perform* 170:108695. <https://doi.org/10.1007/s11665-017-2733-4>
- [22] Li YF, Zhang XX, Li HB (2002) Mixed-phase mullite electrocatalyst for pH-neutral oxygen reduction in magnesium-air batteries. *Nano Energy* 36:265–265. <https://doi.org/10.1016/j.nanoen.2016.06.033>
- [23] Li CS, Sun Y, Gebert F, Chou SL (2017) Current progress on rechargeable magnesium-air battery. *Adv Energy Mater* 7:1700869. <https://doi.org/10.1002/aenm.201700869>
- [24] Zhang JL, Ma JL, Wang GX, Li YQ, Volinsky AA (2019) Electrochemical performance of 1-Ethyl-3-methylimidazolium Bis(Trifluoromethylsulfonyl)Imide ionic liquid as electrolyte for primary Mg-air batteries. *J Electrochem Soc* 166:A1103–A1106. <https://doi.org/10.1149/2.0821906jes>
- [25] Thomas S, Medhekar NV, Frankel GS, Birbilis N (2015) Corrosion mechanism and hydrogen evolution on Mg. *Curr Opin Solid St M* 19:85–94. <https://doi.org/10.1016/j.cossms.2014.09.005>
- [26] Hoshi Y, Takemiya R, Shitanda I (2016) Communication-gas-chromatographic analysis of hydrogen evolved from magnesium electrode during anodic dissolution. *J Electrochem Soc* 163:C303–C305. <https://doi.org/10.1149/2.0761606jes>
- [27] Fajardo S, Frankel GS (2015) Gravimetric method for hydrogen evolution measurements on dissolving magnesium. *J Electrochem Soc* 162:C693–C701. <https://doi.org/10.1149/2.0241514jes>
- [28] Liu X, Liu SZ, Xue JL (2018) Discharge performance of the magnesium anodes with different phase constitutions for Mg-air batteries. *J Power Sources* 396:667–674. <https://doi.org/10.1016/j.jpowsour.2018.06.085>
- [29] Yuasa M, Huang X, Suzuki K, Mabuchi M, Chino Y (2015) Discharge properties of Mg–Al–Mn–Ca and Mg–Al–Mn alloys as anode materials for primary magnesium-air batteries. *J Power Sources* 297:449–456. <https://doi.org/10.1016/j.jpowsour.2015.08.042>
- [30] Zhang T, Tao Z, Chen J (2014) Magnesium-air batteries: from principle to application. *Mater Horiz* 1:196–206. <https://doi.org/10.1039/C3MH00059A>
- [31] Wang L, Wang R, Feng Y, Deng M, Wang N (2017) Effect of Al and Pb contents on the corrosion electrochemical properties and activation of Mg–Al–Pb alloy anode. *J Electrochem Soc* 164:A438–A446. <https://doi.org/10.1149/2.1211702jes>
- [32] Gu XJ, Cheng WL, Cheng SM, Yu H, Wang ZF, Wang HX, Wang LF (2020) Discharge behavior of Mg–Sn–Zn–Ag alloys with different sn contents as anodes for Mg-air batteries. *J Electrochem Soc* 167:020501. <https://doi.org/10.1149/1945-7111/ab6284>
- [33] Wang NG, Wang RC, Feng Y, Xiong WH, Zhang JC, Deng M (2016) Discharge and corrosion behaviour of Mg–Li–Al–Ce–Y–Zn alloy as the anode for Mg-air battery. *Corros Sci* 112:13–24. <https://doi.org/10.1016/j.corsci.2016.07.002>
- [34] Ma J, Zhang Y, Ma M, Qin C, Wang G (2020) Corrosion and discharge performance of a magnesium aluminum eutectic alloy as anode for magnesium-air batteries. *Corros Sci* 170:108695. <https://doi.org/10.1016/j.corsci.2020.108695>
- [35] Feng Y, Lei G, He YQ, Wang RC, Wang XF (2018) Discharge performance of Mg–Al–Pb–La anode for Mg-air battery. *T Nonferrous Metal Soc* 28:2274–2286. [https://doi.org/10.1016/S1003-6326\(18\)64872-1](https://doi.org/10.1016/S1003-6326(18)64872-1)
- [36] Xu C, Fan GH, Nakata Y, Liang X, Chi YQ, Qiao XG, Cao GJ, Zhang TT, Huang M, Miao KS, Zheng MY, Kamado S, Xie HL (2018) Deformation behavior of ultra-strong and ductile Mg–Gd–Y–Zn–Zr alloy with bimodal microstructure. *Metall Mater Trans A* 49A:1931–1947. <https://doi.org/10.1007/s11661-018-4507-5>
- [37] Zhang JH, Liu SJ, Wu RZ, Hou LG, Zhang ML (2018) Recent developments in high-strength Mg–RE-based alloys: Focusing on Mg–Gd and Mg–Y systems. *J Magnes Alloy* 6:177–291. <https://doi.org/10.1016/j.jma.2018.08.001>
- [38] Pourbahari B, Mirzadeh H, Emamy M, Roumina R (2018) Enhanced ductility of a fine-grained Mg–Gd–Al–Zn magnesium alloy by hot extrusion. *Adv Eng Mater* 20:17011171. <https://doi.org/10.1002/adem.201701171>
- [39] Liu X, Xue J (2019) The role of Al₂Gd cuboids in the discharge performance and electrochemical behaviors of AZ31-Gd anode for Mg-air batteries. *Energy* 189:116314.
- [40] Chen XR, Jia YH, Le QC, Wang HN, Zhou X, Yu FX, Atrens A (2020) Discharge properties and electrochemical behaviors of AZ80–La–Gd magnesium anode for Mg-air

- battery. *J Magnes Alloy*. <https://doi.org/10.1016/j.jma.2020.07.008>
- [41] Chen XR, Wang HN, Zou Q, Le QC, Wen CE, Atrons A (2021) The influence of heat treatment on discharge and electrochemical properties of Mg–Gd–Zn magnesium anode with long period stacking ordered structure for Mg-air battery. *Electrochim Acta* 367:137518. <https://doi.org/10.1016/j.electacta.2020.137518>
- [42] Jiao SH, Zheng JM, Li QY, Li X, Engelhard MH, Cao RG, Zhang JG, Xu W (2017) Behavior of lithium metal anodes under various capacity utilization and high current density in lithium metal batteries. *Joule* 2:110–124. <https://doi.org/10.1016/j.joule.2017.10.007>
- [43] Li CQ, Xu DK, Chen XB, Wang BJ, Wu RZ, Han EH, Birbilis N (2018) Composition and microstructure dependent corrosion behaviour of Mg–Li alloys. *Electrochim Acta* 260:55–64. <https://doi.org/10.1016/j.electacta.2017.11.091>
- [44] Wang NG, Li WP, Huang YX, Wu G, Hu MC, Li GZ, Shi ZC (2019) Wrought Mg–Al–Pb–RE alloy strips as the anodes for Mg-air batteries. *J Power Sources* 436:226855. <https://doi.org/10.1016/j.jpowsour.2019.226855>
- [45] Deng M, Höche D, Lamaka SV, Snihirova D, Zheludkevich ML (2018) Mg–Ca binary alloys as anodes for primary Mg-air batteries. *J Power Sources* 396:109–118. <https://doi.org/10.1016/j.jpowsour.2018.05.090>
- [46] Epelboin I, Keddam M, Takenouti H (1972) Use of impedance measurements for the determination of the instant rate of metal corrosion. *J Appl Electrochem* 2:71–79. <https://doi.org/10.1007/BF00615194>
- [47] Wang L, Snihirova D, Deng M, Vaghefinazari B, Zheludkevich ML (2020) Tailoring electrolyte additives for controlled Mg–Ca anode activity in aqueous Mg-air batteries. *J Power Sources* 460:228106. <https://doi.org/10.1016/j.jpowsour.2020.228106>
- [48] Hu Z, Yin Z, Yin Z, Wang K, Liu QD, Sun PF, Yan H, Song HG, Luo C, Guan HY, Luc C (2020) Corrosion behavior characterization of as extruded Mg–8Li–3Al alloy with minor alloying elements (Gd, Sn and Cu) by scanning Kelvin probe force microscopy. *Corros Sci* 176:108923. <https://doi.org/10.1016/j.corsci.2020.108923>
- [49] Arrabal R, Pardo A, Merino MC, Paucar K, Mohedano M, Casajús P, Garcés G (2012) Influence of Gd on the corrosion behavior of AM50 and AZ91D magnesium Alloys. *Corro* 68:398–410. <https://doi.org/10.5006/0010-9312-68.5.398>

Publisher's Note Springer Nature remains neutral with regard to jurisdictional claims in published maps and institutional affiliations.